



<b>Publication Year</b>	2017
<b>Acceptance in OA</b>	2020-11-19T14:22:06Z
<b>Title</b>	Laboratory measurements of super-resolving Toraldo pupils for radio astronomical applications
<b>Authors</b>	OLMI, LUCA, BOLLI, Pietro, CRESCI, Luca, D'Agostino, Francesco, Migliozi, Massimo, Mugnai, Daniela, Natale, Enzo, NESTI, Renzo, PANELLA, Dario, Stefani, Lorenzo
<b>Publisher's version (DOI)</b>	10.1007/s10686-017-9535-4
<b>Handle</b>	<a href="http://hdl.handle.net/20.500.12386/28449">http://hdl.handle.net/20.500.12386/28449</a>
<b>Journal</b>	EXPERIMENTAL ASTRONOMY
<b>Volume</b>	43

## Laboratory measurements of super-resolving Toraldo pupils for radio astronomical applications

Luca Olmi<sup>1,2</sup> · Pietro Bolli<sup>1</sup> · Luca Cresci<sup>1</sup> · Francesco D'Agostino<sup>3</sup> ·  
Massimo Migliozzi<sup>3</sup> · Daniela Mugnai<sup>4</sup> · Enzo Natale<sup>1</sup> · Renzo Nesti<sup>1</sup> ·  
Dario Panella<sup>1</sup> · Lorenzo Stefani<sup>4</sup>

Received: 17 October 2016 / Accepted: 20 March 2017  
© Springer Science+Business Media Dordrecht 2017

**Abstract** The concept of super-resolution refers to various methods for improving the angular resolution of an optical imaging system beyond the classical diffraction limit. Although several techniques to narrow the central lobe of the illumination Point Spread Function have been developed in optical microscopy, most of these methods cannot be implemented on astronomical telescopes. A possible exception is represented by the variable transmittance filters, also known as “Toraldo Pupils” (TPs) since they were introduced for the first time by G. Toraldo di Francia in 1952 (Toraldo di Francia, *Atti Fond. Giorgio Ronchi* **7**, 366, 1952). In the microwave range, the first successful laboratory test of TPs was performed in 2003 (Mugnai et al. *Phys. Lett. A* **311**, 77–81, 2003). These first results suggested that TPs could represent a viable approach to achieve super-resolution in Radio Astronomy. We have therefore started a project devoted to a more exhaustive analysis of TPs, in order to assess their potential usefulness to achieve super-resolution on a radio telescope, as well as to determine their drawbacks. In the present work we report on the results of extensive microwave measurements, using TPs with different geometrical shapes, which confirm the correctness of the first experiments in 2003. We have also extended the

Q1

---

✉ Luca Olmi  
olmi.luca@gmail.com

Q2

<sup>1</sup> Osservatorio Astrofisico di Arcetri, Istituto Nazionale di Astrofisica (INAF), Largo E. Fermi 5, 50125 Firenze, Italy

<sup>2</sup> Physics Department, Rio Piedras Campus, University of Puerto Rico, UPR Station, Box 23343, San Juan, PR, USA

<sup>3</sup> Università di Salerno, Via G. Paolo II 132, 84084 Fisciano, SA, Italy

<sup>4</sup> Consiglio Nazionale delle Ricerche (CNR), Istituto di Fisica Applicata Nello Carrara, Via Madonna del Piano 10, 50019 Firenze, Italy

25 original investigation to carry out full-wave electromagnetic numerical simulations  
26 and also to perform planar scanning of the near-field and transform the results into  
27 the far-field.

28 **Keywords** Angular resolution · Super-resolution techniques · Toraldo pupils ·  
29 Microwave measurements · Near-field

## 30 1 Introduction

31 The concept of super-resolution refers to various methods for improving the angu-  
32 lar resolution of an optical imaging system beyond the classical diffraction limit. In  
33 optical microscopy, several techniques have been successfully developed with the  
34 aim of narrowing the central lobe of the illumination Point Spread Function (PSF).  
35 These techniques either involve changing the fluorescence status of the specimen, or  
36 the specimen is imaged within a region having a radius much shorter than the illu-  
37 mination wavelength, thus exploiting the unique properties of the evanescent waves.  
38 Using electrically small artificial structures, negative refractive index (NRI) metama-  
39 terials (also known as negative index media, or NIM) provide a physical platform to  
40 controlling the properties of electromagnetic (EM) waves. One of the most striking  
41 properties of NRI materials is that a slab of metamaterial can be a “perfect lens” in  
42 which the evanescent waves, instead of decaying, are in fact enhanced through the  
43 slab and in theory it is thus capable of imaging infinite small features of targets [26].

44 However, few efforts have been made to overcome the diffraction limit of tele-  
45 scopes. This is mainly attributed to the fact that remote objects, like astronomical  
46 targets, are not easily accessible for artificial radiation manipulation and the great size  
47 of telescopes reduces the possibility of super-resolution optical elements composed  
48 of metamaterials. A concept that used a NRI lens positioned between the conven-  
49 tional reflector of a radio telescope and its focal plane to shape the PSF has been  
50 proposed [13] but, to our knowledge, there are no published experimental measure-  
51 ments. A more exotic concept based on quantum cloning [9] has also been published,  
52 but its practical realization is yet to be proven.

53 In a classical filled-aperture telescope with diameter  $D$ , and angular resolution  
54  $\simeq \lambda/D$ , the purpose of a super-resolving optical device would be to increase the  
55 resolving power of the telescope without increasing its aperture. In fact, aperture  
56 synthesis telescopes can enhance the angular resolution beyond the limits of its  
57 individual filled-aperture telescopes, but at the cost of much increased complexity.  
58 References [2] and [3] review and discuss methods for designing super-resolving  
59 pupil masks that use *variable transmittance pupils* for optical telescopes. These  
60 pupils are attractive to design antennas and telescopes with resolution significantly  
61 better than the diffraction limit,  $\simeq \lambda/D$ , since their realization does not require sig-  
62 nificant modifications to the optical layout of the telescope or any new technological  
63 breakthrough.

64 The first time such pupils were discussed was at a lecture delivered by Toraldo di  
65 Francia at a colloquium on optics and microwaves in 1952 [23]. Toraldo di Francia  
66 suggested that the classical limit of optical resolution could be improved interposing

a filter consisting of either infinitely narrow concentric rings or finite-width concentric annuli of different amplitude and phase transmittance in the entrance pupil of an optical system. These pupils are now also known as Toraldo pupils (TPs, hereafter) and are considered a special case of a the more general case of variable transmittance pupils. In fact, it can be easily shown that a TP consisting of infinitely narrow concentric rings, or *continuous* Toraldo pupil, is equivalent to a transmittance pupil with a complex illumination function (Olmi et al., in prep.). Many other super-resolving filters have since been proposed, but these methods offer little theoretical advantage over the original method proposed by Toraldo di Francia, as shown in Ref. [4].

TPs have been widely analyzed in the context of microscopy [10, 12, 15], but so far they have never been designed for telescope or antenna applications. In fact, the first experimental studies in the microwave range of a TP were carried out in 2003 [14] and 2004 [20]. These successful laboratory results later raised the interest in the potential application of TPs to microwave antennas and radio telescopes. In fact, given that discrete TPs (i.e., employing finite-width concentric coronae with different complex transmittance) for the microwave range are very easy to fabricate and relatively easy to model, we started a project devoted to a more careful analysis of TPs and how they could be implemented on a radio telescope.

During the first part of this work we have conducted extensive electromagnetic numerical simulations of TPs, using a commercial full-wave software tool, that have already been discussed elsewhere [18]. We have used these simulations to study various EM effects that can mask and/or modify the performance of the pupils and to analyze the near-field (NF) as well as the far-field (FF) response. We then used these EM simulations to prepare more comprehensive laboratory testing, and the purpose of this paper is thus to discuss a series of experimental tests conducted at 20 GHz that significantly extend and improve previous laboratory investigations [14, 20]. Our results again confirm Toraldo di Francia's model and also suggest that TPs should be investigated as a potential tool to achieve super-resolution on a radio telescope.

The outline of the paper is as follows. In Section 2 we give an overview of the basic properties of TPs. In Section 3 we summarize the EM simulations which have been described elsewhere [18] and also discuss some additional EM modeling specific to our laboratory tests. In Section 4 we describe the laboratory setup and procedures used to perform our measurements and the results obtained in the NF using two different types of TP. Therefore, in Section 5 we describe how the NF measurements were converted into the FF. Finally, in Section 6 we draw our conclusions.

## 2 Toraldo pupils

### 2.1 Analytical description

As we earlier mentioned, Toraldo di Francia introduced for the first time the concept of variable transmittance pupils in 1952 [23, 24], and an analytical description of TPs can be found in several references [1, 4, 14]. For the convenience of the reader we briefly review the theory here. In Toraldo di Francia's model several approximations are implicitly assumed, thus reducing the problem of the scattered fields to a scalar

109 diffraction problem in the case of linearly polarized radiation incident on the aperture  
 110 (see, e.g., Chapter 5.14 of Ref. [22]). A full-wave discussion of the scattered fields  
 111 from a TP is beyond the scopes of this work, and therefore we will adopt the same  
 112 approximations as in Toraldo di Francia's original version. However, for the near- to  
 113 far-field transformation described in Section 5 we will adopt the full-wave approach  
 114 both in our laboratory measurements and in the EM simulations.

115 Let us then consider a circular pupil of diameter  $D$  and divide it into  $n$  discrete,  
 116 concentric circular coronae by means of  $n + 1$  circumferences with diameters  $\alpha_0 D$ ,  
 117  $\alpha_1 D, \dots, \alpha_n D$ , where  $\alpha_0, \dots, \alpha_n$  is a succession of numbers in increasing order,  
 118 with  $\alpha_0 = 0$  and  $\alpha_n = 1$ . In Toraldo di Francia's original version, each corona is  
 119 either perfectly transparent or provides a phase inversion (i.e., a  $\Delta\phi = 180^\circ$  phase  
 120 change, see below), and is illuminated by a plane wave (i.e., with uniform phase over  
 121 the pupil). By setting  $x = \pi \frac{D}{\lambda} \sin \theta$ , where  $\theta$  is the angle of diffraction measured  
 122 with respect to the optical axis and  $\lambda$  is the wavelength, it can be shown that the total  
 123 amplitude (in the FF),  $A(x)$ , diffracted by the composite TP is given by:

$$A(x) = \sum_{i=0}^{n-1} \frac{k_{i+1}}{x} [\alpha_{i+1} J_1(\alpha_{i+1}x) - \alpha_i J_1(\alpha_i x)] \quad (1)$$

124 where  $k_{i+1} = \frac{\pi D^2}{2\lambda^2} A_{i+1}$  is a constant that is proportional to the amplitude  $A_{i+1}$   
 125 illuminating each corona, and  $J_1$  is the Bessel function of the first order.

126 Once the partition of the pupil into  $n$  circular coronae is established, we can  
 127 impose  $n$  independent conditions on  $A(x)$ , thus obtaining a system of  $n$  equations  
 128 from which we can determine the coefficients  $k_1, \dots, k_n$ . These equations can be  
 129 obtained, for example, by  $A(x_i) = 0$  where  $x_i$  ( $i = 0 \dots n - 1$ ) represent the zeros  
 130 of the diffracted amplitude. In particular, by setting the position of the first zero the  
 131 user establishes the width of the main lobe and thus the extent of the super-resolution  
 132 effect.

133 Note that the  $k$  coefficients can also have negative values, in which case they  
 134 represent a *phase-inversion* of the wave propagating through the pupil. In fact, in  
 135 this work we are only concerned with the simplest possible pupil, i.e., composed of  
 136 discrete circular coronae that do or do not introduce a phase-inversion. A description  
 137 of continuous phase filters can be found elsewhere [5], as well as their application to  
 138 ground-based telescopes [2], while the precise relation with discrete Toraldo pupils  
 139 will be discussed in a forthcoming paper (Olmi et al., in prep.) . Note that in order  
 140 to obtain the phase-inversion,  $\Delta\phi = (2\pi/\lambda) \Delta l = \pi$ , the optical path *excess* (with  
 141 respect to the wave propagating through air) must be  $\Delta l = l_{\text{diel}} - l_{\text{air}} = (n_{\text{diel}} -$   
 142  $n_{\text{air}}) \Delta s = 0.5\lambda$ , where  $\Delta s$  is the physical thickness of the dielectric material and  $n$   
 143 is the refraction index. If  $n_{\text{diel}} \simeq 1.5$  and  $n_{\text{air}} \simeq 1$  then  $\Delta s \simeq \lambda$ .

## 144 2.2 Illumination of the pupil

145 Solving the set of equations  $A(x_i) = 0$  allows to determine the  $k_i$  coefficients and  
 146 thus, given that they are proportional to the amplitude  $A_i$  illuminating each corona,  
 147 it also determines the type of amplitude *apodization* required by a specific TP. In  
 148 general, if no *a priori* constraint on the illumination is set, the resulting apodization

may be quite complex, and while at visible wavelengths the required amplitude distribution could in principle be obtained using the appropriate neutral filters, in the microwave range this technique is not easily implemented. For example, in Ref. [18] it is shown that for the simple case of a 3-coronae TP, its geometry can be chosen so that the required intensity illumination at the center of each corona can be adequately fit by a Gaussian beam. At microwave wavelengths a Gaussian illumination can be easily obtained using, for example, a rectangular feedhorn but a Gaussian beam cannot provide a uniform phase over the pupil, which is one of the optical conditions required by a TP. The pupil could be located in the FF of the Gaussian beam source, where the spherical wavefront can be approximated as a plane wave over the extent of the pupil, thus satisfying the uniform phase condition but without the required amplitude apodization.

Since it appears very difficult to implement amplitude apodization and uniform phase simultaneously over the pupil it is of interest to analyze how the output amplitude from a TP would change if one of these conditions is not met. For example, if the phase inversion, corresponding to negative  $k$  coefficients, is *not* applied then no super-resolution effect is achieved and the shape of the PSF is basically unchanged. Instead, the condition about the amplitude apodization can be relaxed, though at the cost of a mild reduction in the super-resolution effect and modified sidelobes.

The simple case of a 3-coronae TP has been discussed elsewhere [18], and we thus show the equivalent effects for the case of a 4-coronae TP in Fig. 1. For this specific example we have selected the  $\alpha$  coefficients as  $\alpha = [0, 0.16, 0.4, 0.8, 1]$ . Given that an open pupil with the same diameter has its first zero at  $x = 3.83$  (corresponding to  $\sin \theta = 1.22\lambda/D$ ) we set the amplitude  $A(x_i) = 0$  at the values of  $x = [3, 4, 5]$ , thus narrowing the main lobe, and we also set the maximum value of  $A$  at  $x = 0$ . The

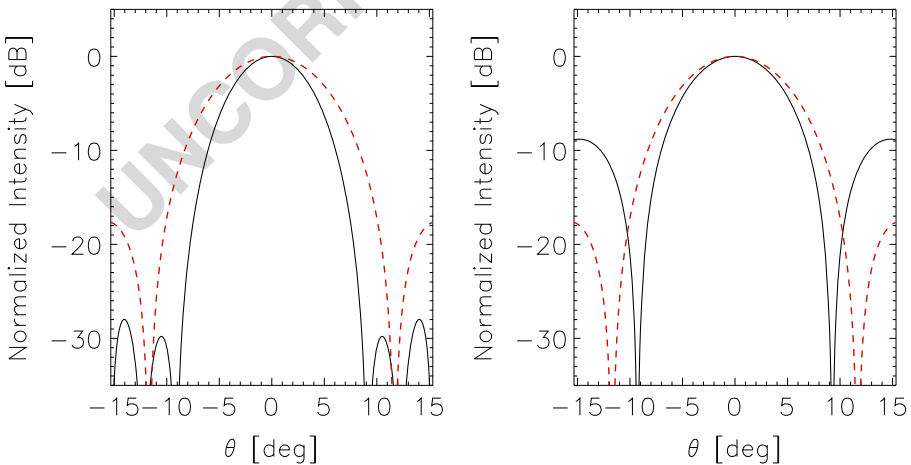


**Fig. 1** *Left panel.* Diffraction pattern at  $\nu = 20$ GHz by a four-coronae TP, as given by the square of (1) for  $n = 4$  (black solid line), and that of a normal pupil of equal diameter (red dashed line). Both curves are normalized with respect to the on-axis value. The correct amplitude apodization has been applied resulting in an angular resolution gain  $G = 1.94$ . *Right panel.* Normalized diffraction pattern at  $\nu = 20$ GHz assuming the correct phase distribution but with no amplitude apodization, resulting in  $G = 1.65$

174 resulting (unnormalized)  $k$  coefficients are  $k = [-778.2, 264.5, -40.8, 22.9]$ . The  
175 left panel of Fig. 1 shows the calculated diffracted amplitude by the TP assuming the  
176 correct amplitude apodization and phase inversion. It is customary [4] to define the  
177 resolution gain,<sup>1</sup>  $G$ , as the ratio of the radius of the first zero of the Airy distribution  
178 to that of the super-resolving diffraction pattern. Here we replace the radius of the  
179 first zero with the full width at half-maximum (FWHM, corresponding to the width  
180 at  $-3$  dB with respect to the peak value) of the PSF to measure  $G$ , which in this case  
181 is  $G = 1.94$ . In the right panel of Fig. 1 we show the diffracted amplitude with *no*  
182 amplitude apodization applied, but still with the correct phase relations. The relative  
183 intensity, number and position of the sidelobes have changed and the super-resolution  
184 effect is somewhat lower, with  $G = 1.65$ .

185 This example shows that, although the super-resolution effect is still present, the  
186 performance of a TP is different if the correct apodization condition is not applied,  
187 which makes these pupils difficult to study in the microwave range with EM numer-  
188 ical simulations (see Section 3). Likewise, testing TPs in the laboratory would in  
189 principle require to design a suitable method to implement both amplitude apodiza-  
190 tion and phase inversions. However, in Section 4 we show that successful results can  
191 also be obtained when amplitude apodization is not present. These problems could be  
192 partly resolved with the use of phase-only masks [5, 11] which will also be discussed  
193 in a future work (Olm et al., in prep.).

## 194 3 Electromagnetic simulations

### 195 3.1 Summary of previous results

196 Any measurement performed in the laboratory cannot fully satisfy all of the opti-  
197 cally ideal conditions which are assumed for a TP, and thus a way to validate and  
198 test the performance of a TP under less than ideal laboratory conditions is required.  
199 The method used must also be able to address how the theoretical performance of a  
200 TP can be masked or altered by various optical (mostly diffractive) effects. There-  
201 fore, we carried out an extensive series of EM numerical simulations using the  
202 commercial software FEKO,<sup>2</sup> a comprehensive EM simulation software tool for the  
203 electromagnetic field analysis of 3D structures.

204 After a few attempts with frequencies,  $\nu$ , of 10 and 50 GHz, we decided to per-  
205 form the bulk of the EM simulations, followed by laboratory measurements, at  
206  $\nu = 20$  GHz. At lower frequencies the computing time would be much lower, but  
207 the size (and separations) of the optical elements in units of wavelengths would  
208 be uncomfortably large for our expected experimental setup. At higher frequencies  
209 the situation pretty much reverses, with far too long computing times though with

---

<sup>1</sup>Not to be confused with the *antenna* gain.

<sup>2</sup><http://www.altairhyperworks.com/product/FEKO>.

the advantage of reasonably sized microwave components. We found that 20 GHz represents a good trade-off between these opposite requirements.

During the first part of this work our EM simulations had the main purpose of generating a FEKO model which would represent an optical configuration as close as possible to the ideal system described in Section 2, thus trying to simulate the performance predicted by (1). These numerical simulations have already been discussed in a previous work [18], and thus here we just present a brief summary of the main results:

1. Two different sources have been tested: plane-wave and Gaussian-beam illumination. The use of plane-waves requires a special technique to simulate an infinite ground plane where the pupil is realized, in order to avoid strong diffraction effects from the edges of a finite surface.
2. The Gaussian beam produced by a rectangular feedhorn must illuminate the pupil in the FF to ensure the uniform phase condition. The tapered illumination of the feedhorn can also be used with a finite ground screen.
3. Both NF and FF distributions have been analyzed. However, the analytical model of a TP discussed in Section 2.1 can only be compared with the FF numerical results.
4. The simulated FFs confirm the super-resolution effect, even with no amplitude apodization. They also show that TPs with different numbers of coronae can be used to achieve a trade-off between resolution gain,  $G$ , strength and position of the side lobes, and overall efficiency, measured as the decrease of the on-axis intensity compared to the open pupil.

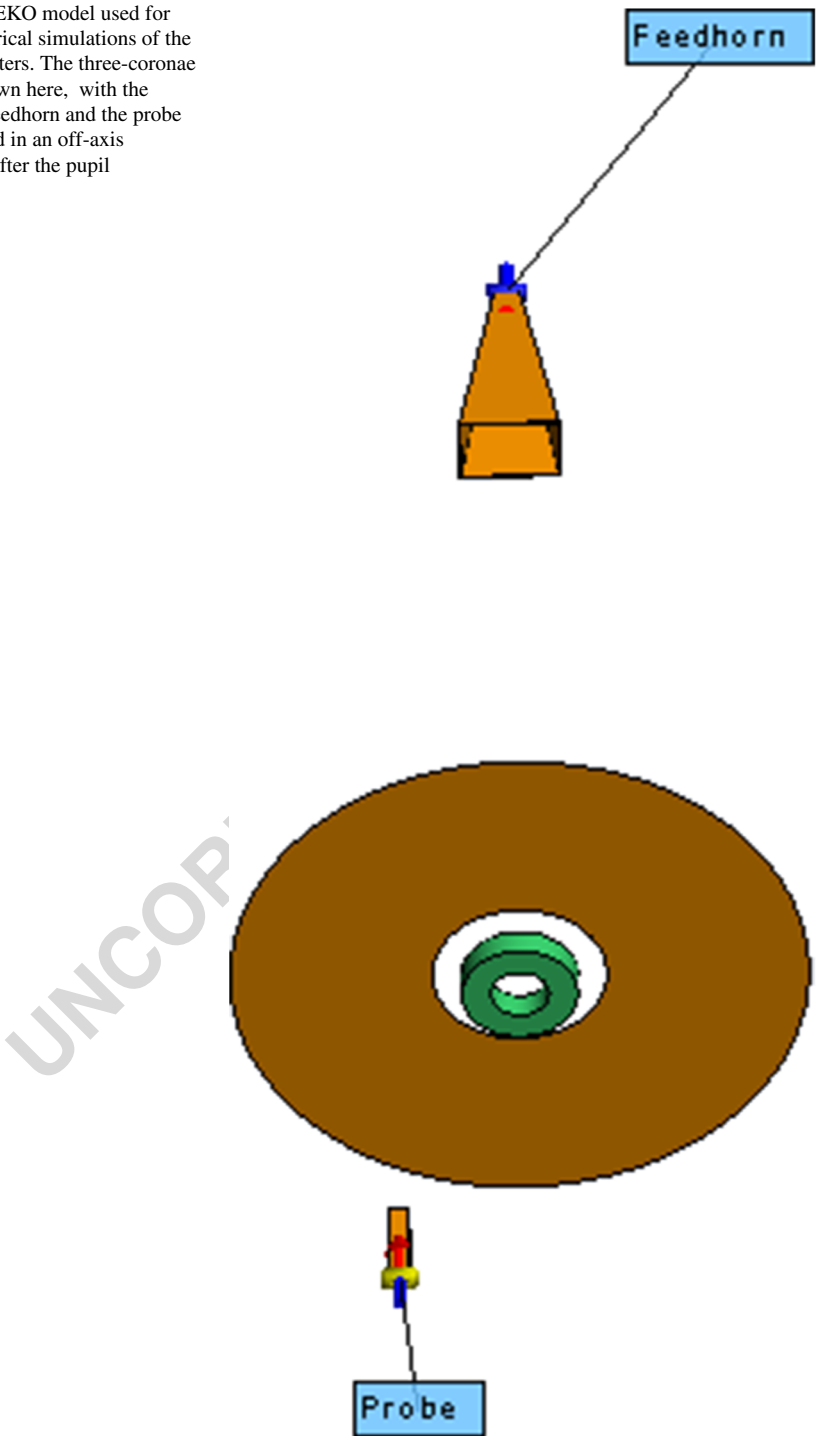
Our initial EM simulations were thus successful, and helped us to analyze both the super-resolution effect using various geometrical configurations, and also other diffraction effects that could mask the expected narrowing of the PSF. Although simulating the FF is in general easier and less time-consuming than computing the NF, we were expecting to perform our experimental measurements in the NF (see Section 4.1). Therefore, we also carried out a number of EM simulations of the NF that were more closely reproducing the laboratory conditions, which we describe in the next section.

### 3.2 Numerical simulations for S-parameters

One of the main goals of this work was to compare our experimental measurements in the NF with the expected results from our EM simulations. However, in this respect the main limitation of the EM simulations summarized above and discussed in Ref. [18] is that they used an incident plane wave as the illuminating source. Furthermore, these simulations sampled the NF point-by-point, without taking into account the finite spatial response of the NF probe used in the actual measurements. Hence, the only viable option to perform a more reliable comparison between the measured and simulated diffraction patterns in the NF was to include the NF probe as well as the feedhorn in the FEKO model.

**Fig. 2** FEKO model used for the numerical simulations of the *S*-parameters. The three-coronae TP is shown here, with the on-axis feedhorn and the probe positioned in an off-axis position after the pupil

Q3



Therefore, we built a FEKO model specific for the NF measurements, that included both the feedhorn as the launcher and the probe after the pupil to sample the NF. Figure 2 shows our model where the feedhorn is visible behind the three-coronae pupil and the NF probe can be seen in front of the screen, in an off-axis position. In this case, since the field detection is done only through the excitation of the waveguide, the EM simulation returns the values of the scattering parameters, or  $S$ -parameters, which measure the reflection and transmission coefficients of a 2-port device, such as a Vector Network Analyzer (VNA). During this simulation, the distances of the feedhorn and the probe to the pupil are held fixed, while the probe is moved perpendicular to the optical axis at regular steps. The forward and reverse transmission coefficients,  $S_{21}$  and  $S_{12}$ , are calculated, and once they are normalized they can be plotted as a function of the scanning position to be compared with the measured normalized NF diffraction pattern. This comparison will be discussed later in Section 4.2.

During the numerical simulations we found that diffraction by the edges of the disk where the circular aperture is realized could cause anomalous amplitudes along the optical axis. Since this effect is not observable off-axis, we think that this may be a consequence of the circular symmetry of the system causing the diffracted waves from the disk edge to interfere on the optical axis. This effect is geometry-dependent, and thus we chose the radius of the disk and the distance of the probe from the disk so that we did not detect this effect.

## 4 Experimental results 272

### 4.1 Preliminary tests 273

Our experimental measurements had two main goals: (a) detect and quantify the super-resolution effect with at least two TPs having different geometrical shapes; and, (b) evaluate and possibly reduce some of the effects that can mask and/or alter the super-resolution effect. An additional goal consisted in the determination of the FF patterns from NF measurements. In fact, for a circular aperture 9 cm in diameter, such as the one used in our tests, the Fraunhofer distance,  $2D^2/\lambda$ , is about 1 m. We therefore decided to perform NF measurements instead of FF measurements for several reasons: (i) the Fraunhofer distance is of the same order of magnitude as the length of the anechoic chamber (about 7 m); (ii) FF scanning techniques would require more complex and expensive mechanical and microwave equipment, as well as measuring methods; (iii) our preliminary tests indicated that we did not have enough sensitivity to make measurements of the diffracted FF at distances of a few meters; (iv) the FF would be severely affected by diffraction effects caused by the ground screen supporting the TP, unless a much larger screen was adopted.

We note that these requirements are specific to our laboratory setup. On a telescope the TP, like any other optical device designed to modify the incident plane wavefront, should ideally operate at the entrance pupil of the telescope, i.e., the primary mirror. For antennas and telescopes where this is not possible, an image of the entrance pupil can be used to place a transmittance filter [17].

## 293 4.1.1 Measurement setup

294 All microwave components were mounted on vertical supports that allowed to raise  
295 the optical axis about 1.5 m above the ground, in order to minimize the effects of  
296 reflections and multiple scatterings from the ground and the optical bench, though  
297 covered with microwave absorbers. The optical bench, 2.5 m long (see Fig. 3) allowed  
298 all vertical supports to move along the direction of propagation, which we will  
299 indicate as the  $z$ -axis.

300 All measurements were performed with a VNA (Anritsu 37277C) recording both  
301 amplitude and phase. Coaxial cables connected the VNA to the launcher, a rectangu-  
302 lar feedhorn having a mouth  $4 \times 5.5$  cm in size, while the waveguide had dimensions  
303  $1.07 \times 0.43$  cm with a total length of 11 cm. The horn had a taper of  $-3$  dB at an  
304 angle of  $\simeq 9$  deg (FWHM = 18 deg) with respect to the optical axis, and a gain of  
305  $\simeq 20$  dB. The NF probe consisted of a section, 18 cm in length, of an open-ended  
306 waveguide WR42 with smooth edges. Both the feedhorn and the probe were aligned  
307 so that their  $E$ -field was directed vertically, or along the  $y$ -axis, according to Fig. 4.  
308 The probe was mounted on a manual translational stage to scan the NF on an axis per-  
309 pendicular to the direction of propagation (see Fig. 3). In between the feedhorn and  
310 the probe was mounted an assembly supporting a metal ground screen with a circular  
311 aperture which allowed to mount and remove the TPs. This assembly was covered by  
312 thin ( $\simeq 1$  cm thick) planar microwave absorbers on the side facing the feedhorn. A  
313 schematics of the test set-up is shown in Fig. 4.

314 After warm-up, both phase and amplitude measured with the VNA remained quite  
315 stable with peak-to-peak variations  $\lesssim 0.1$  dB for the amplitude and  $\lesssim 0.5$  deg for the  
316 phase. The feedhorn and the probe were first aligned using a HeNe laser positioned  
317 behind the horn. The circular aperture with the TP was then added to the optical  
318 bench and aligned as well. The coplanarity of the mouth of the horn and the plane of  
319 the circular aperture was checked using a retroreflector.



**Fig. 3** Experimental setup for our laboratory tests at  $\nu = 20$  GHz. The launcher (rectangular feedhorn) is visible to the left, surrounded by absorbing cones. On the right one can see the screen with the circular hole holding the TP and behind it the NF probe mounted on a linear stage to scan the field on an axis perpendicular to the direction of propagation,  $z$ . Later, the linear stage has been replaced with a two axis translation stage. All components are mounted on vertical supports that can be moved along  $z$  on an optical bench set on the ground, which is covered with absorbing panels in this picture

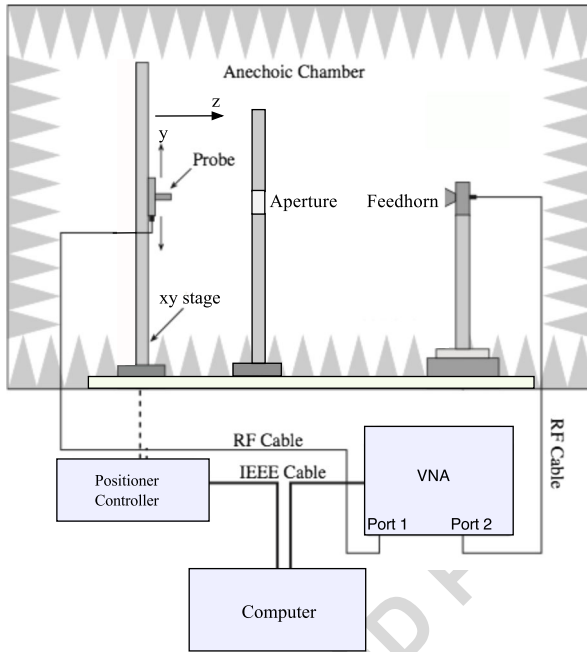


**Fig. 4** Schematics of the NF measurement system

4.1.2 Noise measurements

320

After the initial setup, we proceeded to measure the RF alignment and the noise level, both in amplitude and phase. We carried out these tests with just the launcher and the probe. The probe was decentered manually to scan the field from  $-5$  to  $+5$ cm in the horizontal direction,  $x$ , perpendicular to the optical axis,  $z$ . The horizontal scan was repeated five different times, and the mean and standard deviation of both amplitude and phase were estimated for each probe position (see Fig. 5). The amplitude is quite uniform along  $x$ , with peak-to-peak variations of less than  $0.15$  dB.

321  
322  
323  
324  
325  
326  
327

The power pattern of the feedhorn is expected to decrease as  $P/P_o = \exp[-0.5(\theta/\sigma)^2]$ , where  $P_o$  represents the on-axis power level,  $\theta$  is the angle of observation measured with respect to the optical axis and  $\sigma = \theta_{FWHM}/2.3548$ . Thus, the expected power (or amplitude) variation at  $x = \pm 5$  cm is  $-0.002$  dB, and we note that the observed amplitude variation along the  $x$ -axis in the top panel of Fig. 5 is well within the error bars of the single measurement. These non-repeatable errors are due to various sources of scattering within the anechoic chamber which limit our ability to measure amplitude variations  $\lesssim 0.05 - 0.1$  dB. Further tests have shown that we can appreciate amplitude variations ( $\gtrsim 0.1$  dB) along the scan axis if the separation between the feedhorn and the probe is  $\lesssim 1.8$  m. However, the bottom panel of Fig. 5 shows that we can measure phase variations with greater accuracy. At a distance of  $\simeq 2$  m the spherical wavefront propagating from the feedhorn should cause a phase variation of about  $11$  deg at  $x = \pm 5$  cm, and this is approximately what we

328  
329  
330  
331  
332  
333  
334  
335  
336  
337  
338  
339  
340

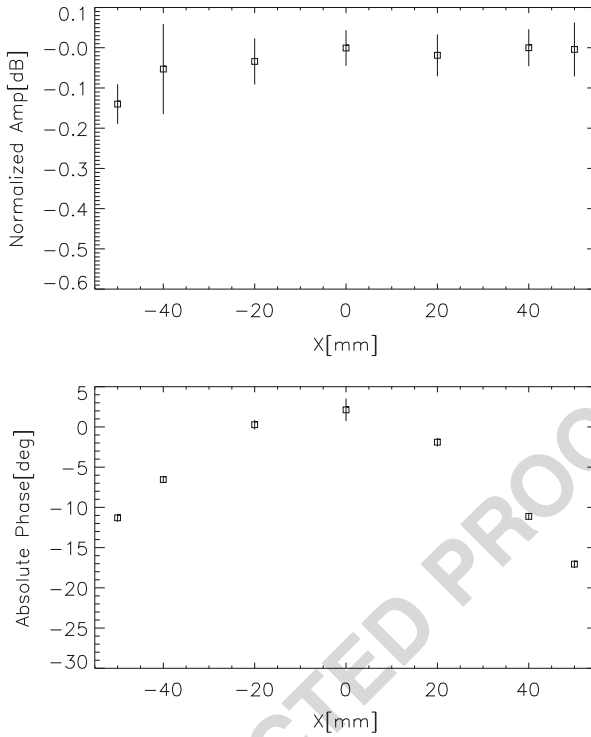


**Fig. 5** *Top panel.* Measured normalized amplitude at  $\nu = 20$  GHz as a function of position along the horizontal direction,  $x$ , perpendicular to the optical axis (located at  $x = 0$ ). The probe was set at a distance along  $z$  of 2 m from the feedhorn. *Bottom panel.* Same as the top panel for the phase. The error bars have roughly the same size as the symbol

341 see in Fig. 5. The slightly different phase variation at  $x = -5$  cm and  $x = +5$  cm  
 342 is a measure of the RF misalignment.

343 **4.2 Linear scanning in the near-field**

344 After the preliminary tests were completed we proceeded with the measurements of  
 345 the diffracted fields by the open circular pupil and the same three- and four-coronae  
 346 TPs described in Ref. [18]. Figure 6 shows the layout of these TPs, which were  
 347 fabricated from low-loss polyethylene, having a relative dielectric constant  $\epsilon_r = 2.28$   
 348 and a loss tangent of  $\tan \delta \simeq 3.8 \cdot 10^{-4}$  [6].

349 A scan along the  $x$ -direction was first performed for the open pupil, roughly  
 350 between  $x = -10$  cm and  $x = +10$  cm, with the probe positioned at different  
 351 distances from the screen. In the top panel of Fig. 7 we show an example of our  
 352 results obtained using the three-coronae TP with a distance between the launcher  
 353 and the screen of 1.9 m, while the separation between the screen and the probe was  
 354 18 cm. Even a simple linear scan like this clearly shows that the FWHM of the  
 355 amplitude distribution generated by the TP is smaller than that of an open pupil with the same

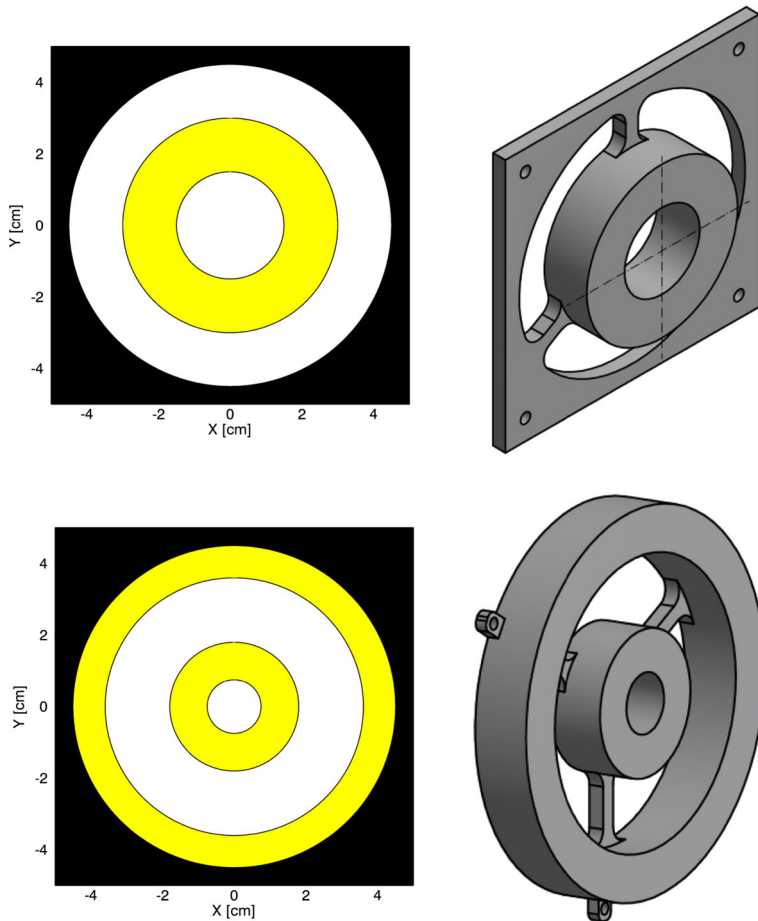


**Fig. 6** *Top panels.* Schematics of a TP with three-coronae (*left*), whose radii are 1.5, 3.0 and 4.5 cm. The corona in the *middle* (in yellow) is the one providing the phase inversion. In the *right panel* we show the CAD drawing used for the fabrication of this TP using low-loss polyethylene. The thickness of the cylinder required to achieve the phase inversion is 1.5 cm. *Bottom panels.* Same as above for the TP with four-coronae. The radii of the four coronae are 0.75, 1.55, 3.60 and 4.50 cm

diameter, and thus we detect the super-resolution effect, at least in the NF. Later we will show that this relation also holds in the FF. We note that the open pupil and TP fields have been measured more extensively on the negative  $x$ -direction. This extended scan was intended to record the sidelobes level and also to check the measurement setup with low signal levels. Several combinations of distance between the launcher and the screen, and separation between the screen and the probe were experimented. The bottom panel of Fig. 7 was in fact obtained using a different set of parameters.

The top-panel of Fig. 7 also shows the radiation diagram obtained with FEKO using the  $S$ -parameters method described in Section 3.2 (the few points shown are

356  
357  
358  
359  
360  
361  
362  
363  
364  
365

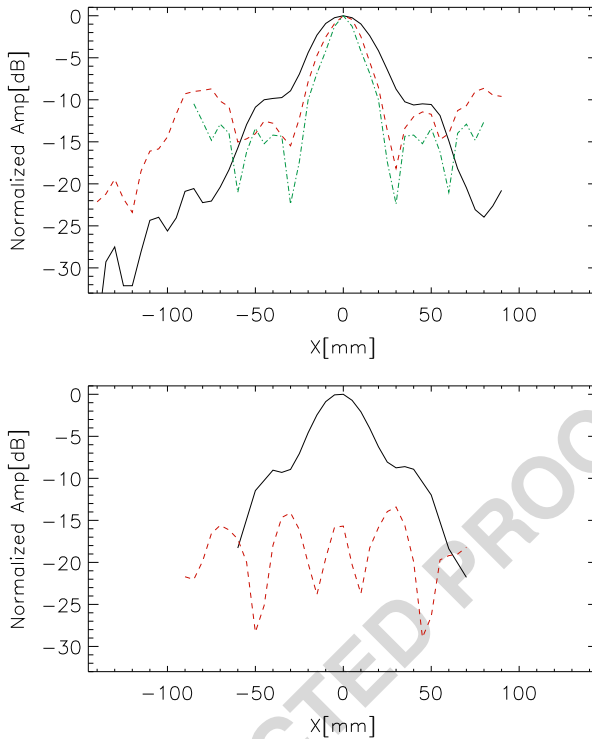


**Fig. 7** *Top panel.* Plot of the amplitude at 20 GHz in the NF of the open pupil (solid, black line), and of the three-coronae TP shown in Fig. 6 (dashed, red line). More measurements were performed on just one side of the scan (the negative  $x$  direction), in order to test the strength of the far sidelobes. For comparison, the simulated amplitude distribution from FEKO, as discussed in Section 3.2, is also shown (dot-dashed, green line). All curves are normalized with respect to the peak value. The distance between the launcher and the screen was 1.9 m, the separation between the screen and the probe was 18 cm, and the sampling interval along the scan direction was 0.5 cm. *Bottom panel.* Same as above for the four-coronae TP. The distance between the launcher and the screen was 1.7 m, the separation between the screen and the probe was 16 cm, and the sampling interval along the scan direction was 0.5 cm. In this case the amplitude generated by the TP is normalized to the peak value of the open pupil

366 due to the long time required by each separate simulation). We note that the simulated  
 367 pattern has a close correspondence with the measured signal, particularly regarding  
 368 the positions of the nulls and the first sidelobes. Both diffraction patterns are sparsely  
 369 sampled and thus part of the discrepancies between the two curves is likely a result of  
 370 the insufficient sampling. It should also be noted that the radiation diagram produced  
 371 by the TP in Fig. 7 also includes the effects of the three small rods that are used  
 372 to hold the dielectric cylinder of the TP connected to the external rim, as shown in the  
 373 right panel of Fig. 6. However, we have performed FEKO simulations including the  
 374 rods and we have verified that the diffraction effects introduced by these supports are  
 375 negligible.

376 The bottom panel of Fig. 7 shows the radiation diagram obtained with the four-  
 377 coronae TP. Since in this case the amplitude generated by the TP is normalized to the

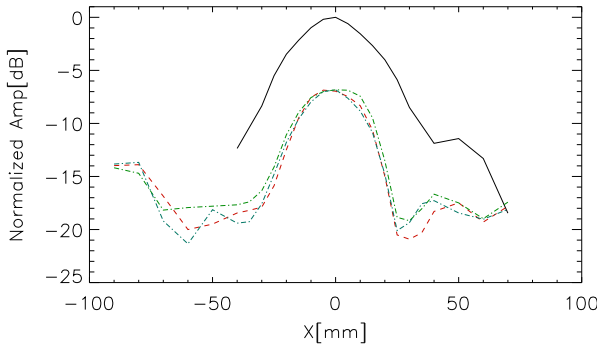


**Fig. 8** Frequency response of the three-coronae TP. The NF of the open pupil is also represented by the solid, black line, while the dashed and dot-dashed lines represent the fields of the TP at 19.84, 20.0 and 20.24 GHz, normalized with respect to the peak value of the open pupil so the actual amplitude decrease is visible. The launcher and probe distance from the pupil plane were 1.7 m and 20 cm, respectively, while the sampling interval was 1.0 cm instead of 0.5 cm as in Fig. 7

peak value of the open pupil, one can appreciate the general decrease of the signal level in the NF when the TP is mounted on the circular aperture. While the central lobe shows the super-resolution effect, the relative level of the sidelobes is much higher compared to the three-coronae TP. Note that the individual FWHM cannot be compared between the top and the bottom panels because the separations between launcher, pupils and probe were different.

Finally, a critical question to be analyzed is the frequency response of a TP, which is important in the perspective of its possible use on a radio telescope. A wide-bandwidth analysis of the TPs was out of the scopes of this work. However, we have performed a simple test by measuring the response of the three-coronae TP at three separate frequencies, specifically 19.84, 20.0 and 20.24 GHz, thus spanning a 400 MHz range. The results are shown in Fig. 8, where all curves are normalized with respect to the peak value of the open pupil so the actual amplitude decrease when using the TP is visible. The launcher and probe distance from the pupil plane were slightly different from the example discussed above, but this has no effect on the present discussion. We note that the main lobes at the three frequencies are quite similar, while most of the differences are limited to the sidelobes. The sampling interval along the scan direction was larger compared to the previous example, and this may also contribute to some of the discrepancies, especially at low signal levels. These measurements suggest that the three-coronae TP has a usable bandwidth  $\gtrsim 400$  MHz. Given that most K-band receivers on currently operating radio telescopes have instantaneous bandwidths  $\sim 1 - 2$  GHz, a TP device might be partially limiting the available bandwidth.

### 4.3 Planar scanning setup

After the preliminary measurements were completed, the NF probe was mounted on a motorized, two axes translation stage, which could be remotely controlled to move the probe at the required position in the  $x - y$  plane, thus performing a *planar*

405 *scanning* of the NF with uniform sampling step (plane-rectangular scanning). Like-  
406 wise, the feedhorn was mounted on a rotational stage, a feature that was required to  
407 precisely rotate the horn and measure the cross-polarization.

408 In preparation for the measurements, the RF absorbing panels were appropriately  
409 positioned all around the metallic structure of the 2D positioner. The usual optical and  
410 RF alignment were then performed. Both VNA and translation stage were remotely  
411 controlled through LabVIEW.<sup>3</sup> The operator would specify the  $x$ - $y$  size and step of  
412 the planar scanning to be performed by the probe in the NF and the control software  
413 would then move the probe at each position in the grid, where it would stop while the  
414 VNA measurement is acquired, and then would move to the next position. A typical  
415 raster map with  $31 \times 31$  points and a 0.5 cm sampling interval would take  $\simeq 1$  hr to  
416 complete. The complex voltage samples are stored together with their positions and  
417 will later be used for the NF-to-FF conversion (see Section 5).

#### 418 4.4 Measurements results

419 Raster maps were performed with the open pupil and with both three- and four-  
420 coronae TPs. If the incident field over the aperture is linearly polarized (see  
421 Section 4.1.1), then in the scalar diffraction approximation (see Section 2.1) we need  
422 to consider only the scattered fields along the polarization direction [22]. However,  
423 because we also required to perform the NF-to-FF transformation (see Section 5),  
424 both our measurements and EM simulations had to determine the copolar and cross-  
425 polar<sup>4</sup> radiation patterns of the scattered fields. In addition, the comparison of  
426 copolar and cross-polar components also had an interest in preparation to a potential  
427 application of TPs with the receiver system of a radio telescope.

428 The cross-polar pattern was recorded after rotating the feedhorn by  $90^\circ$ . The major  
429 challenge for the measurement of the cross-polar pattern was clearly the low-level  
430 of the signal, since we were approaching the expected dynamic range limit of our  
431 experimental setup. For this reason we selected the distance between the feedhorn and  
432 the pupil, and the distance between the pupil and the probe to achieve an acceptable  
433 trade-off in terms of planarity of the incident wave and signal levels, that would  
434 allow the cross-polarization to be measured. We performed planar scannings using  
435 various distances between the probe and the pupil. However, in the end we selected a  
436 separation of 10 cm because larger separations would also lead to a larger truncation  
437 error (see Section 5).

438 The copolar and cross-polar amplitude patterns of the open circular pupil are  
439 shown in Fig. 9. The copolar pattern has a slightly elliptical shape which, however is  
440 not visible in Fig. 10 and is only partially visible in Fig. 11. We do not have enough  
441 data to further investigate this issue, which might be a consequence of the overall  
442 accuracy of the measurement procedure. The cross-polar pattern also shows a good  
443 signal-to-noise ratio (SNR), which allows to measure its level at least 27 dB below

<sup>3</sup><http://www.ni.com/labview/>.

<sup>4</sup>Although the copolar and cross-polar terms are generally referred in the literature to the FF, here we will use them to indicate the vertical,  $y$ -component, and horizontal,  $x$ -component, of the NF.

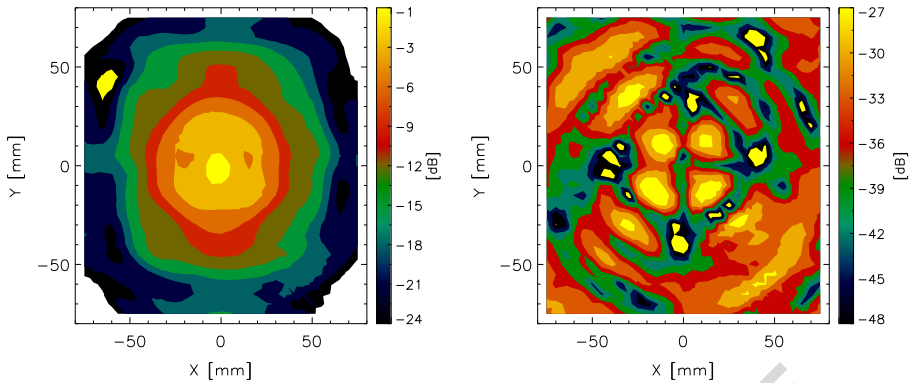


**Fig. 9** *Left panel.* Near-field copolar amplitude distribution at 20 GHz generated by an open circular pupil with diameter 9 cm, at a distance of 10 cm from the plane of the pupil. The launcher was at a distance of 1.7 m from the plane of the pupil. The high-signal spot in the top-left of the map is likely to be an artifact, since it does not show up in subsequent maps. *Right panel.* Same as the left panel for the cross-polar component. The maps are normalized to the peak amplitude value of the copolar pattern

the copolar signal. Achieving a good SNR is a necessary condition in order to allow a reliable reconstruction of the FF. As a repeatability test, we have performed this map again after several days and found that the shape of the pattern was essentially the same, confirming the robustness of the measurements setup.

Next, we have performed the raster map with the three-coronae TP mounted on the circular aperture. The copolar and cross-polar amplitude patterns are shown in Fig. 10. The left panel shows a nicely circular main lobe and a first sidelobe with also an approximately circular symmetry, which indicate a good overall RF alignment. The cross-polar map in the right panel of Fig. 10 also shows the typical four-lobe pattern, but with clearly lower SNR compared to Fig. 9. It should be noted, in fact, that the 0 dB signal level is referred to the peak value of the copolar component of the TP and not of the circular aperture, and thus the absolute amplitudes in Fig. 10 are many dBs below the levels of Fig. 9. In addition, the copolar pattern has a FWHM

444  
445  
446  
447  
448  
449  
450  
451  
452  
453  
454  
455  
456

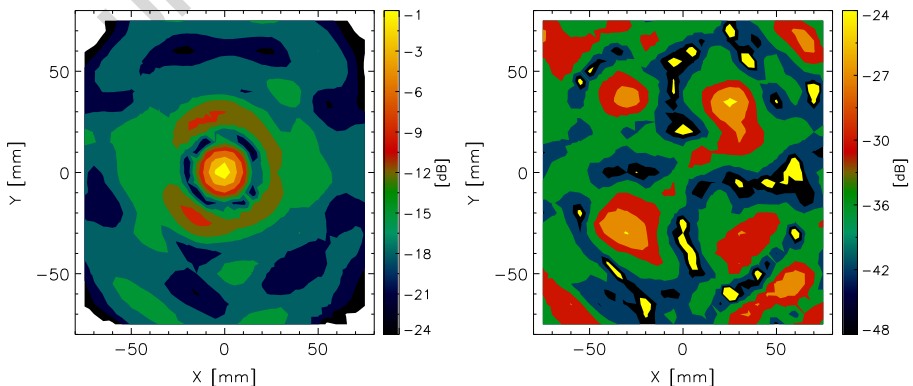


**Fig. 10** Same as Fig. 9 for the three-coronae TP

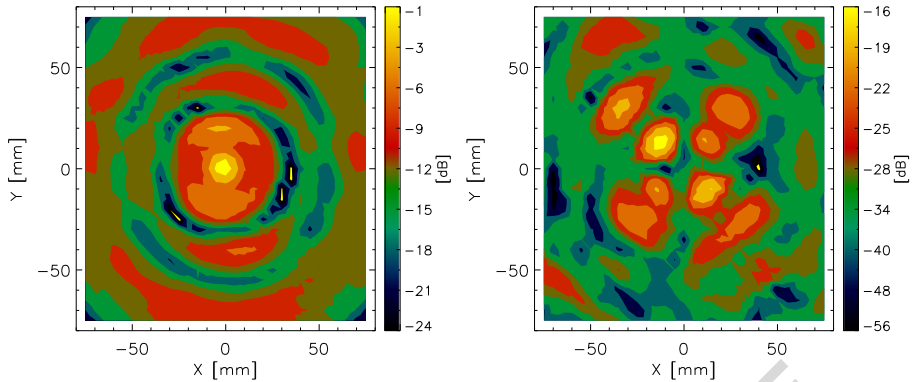


**Fig. 11** Same as Fig. 9 for the four-coronae TP

457 that is clearly smaller than that of the open pupil, which confirms the preliminary  
 458 results described in Section 4.2.

459 Finally, the NF maps obtained with the four-coronae TP are shown in Fig. 11.  
 460 Compared to Fig. 9 the super-resolution effect is clearly visible, but a higher degree  
 461 of asymmetry can be seen in the copolar pattern, which also shows higher sidelobes  
 462 compared to the three-coronae TP. Higher sidelobes were already measured during  
 463 the preliminary linear scans, as shown in Fig. 7. The cross-polar pattern is also clearly  
 464 detected with the same symmetry as in Figs. 9 and 10.

465 In Fig. 12 we also show the transversal cuts, along the  $x$ - and  $y$ -axis, of the 2D  
 466 amplitudes shown in Figs. 9 and 10. These curves should be compared with the top  
 467 panel of Fig. 7. Despite the difference in the FWHM of the  $x$ - and  $y$ -cuts of the  
 468 amplitude of the open pupil, due to the slight asymmetry discussed earlier, these  
 469 results show otherwise a good agreement with the linear scan shown in Fig. 7.

## 470 5 Near-to-far-field transformation

471 Since all our measurements were performed in the NF of the open or composite  
 472 circular pupil, a fundamental step in our work was the determination of the FF pattern  
 473 from the NF measurements. As it was earlier mentioned in Section 4.3, in preparation  
 474 for our NF-FF transformation procedure, we employed a planar scanning technique  
 475 with regularly spaced data (plane-rectangular scanning). This is certainly the simplest  
 476 technique from the experimental and computational point of view, and in Appendix A  
 477 we review the specific method used for the NF-FF transformation. We apply the NF-  
 478 FF transformation to the measured NF of the open and composite circular pupils,  
 479 shown in Figs. 9–11.

480 We show the FF of the three- and four-coronae TP in Figs. 13 and 14, respectively,  
 481 where they are also compared with the FF of the open pupil. We separately show the  
 482 two components along the  $E$  and  $H$  reference planes, which correspond to cuts of

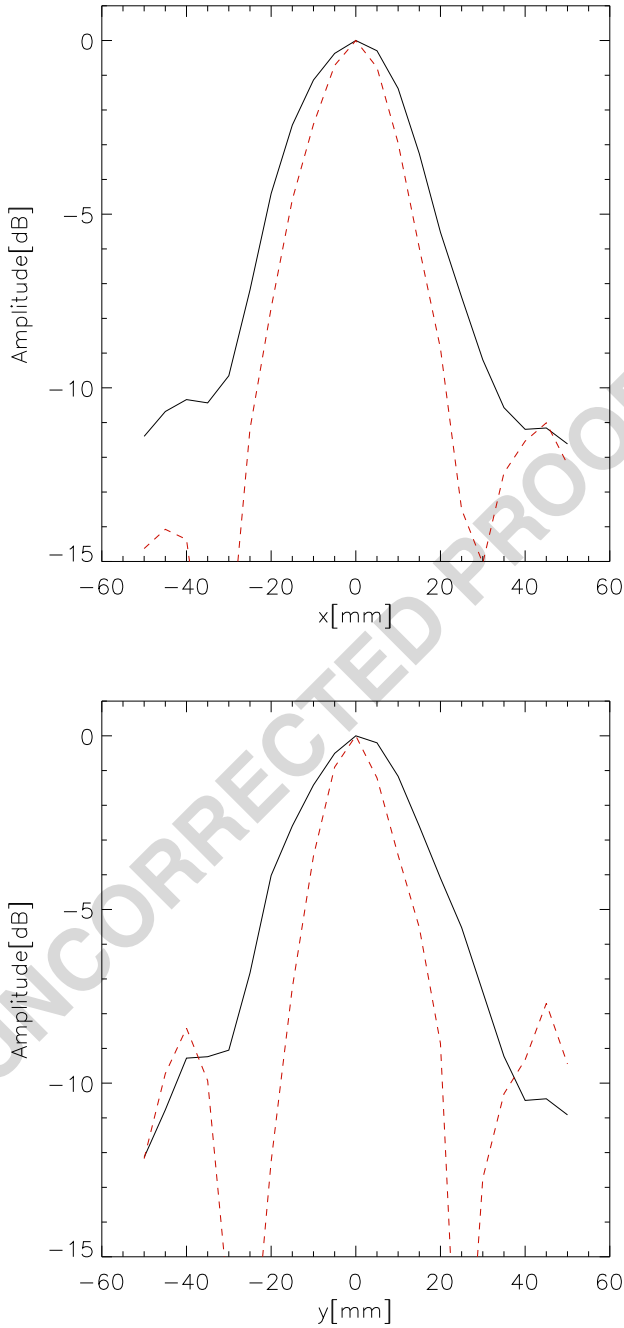


**Fig. 12** 1D cuts of Figs. 9 and 10 along the  $x$ - (*top panel*) and  $y$ -axis (*bottom panel*). Both amplitudes are normalized to their peak values

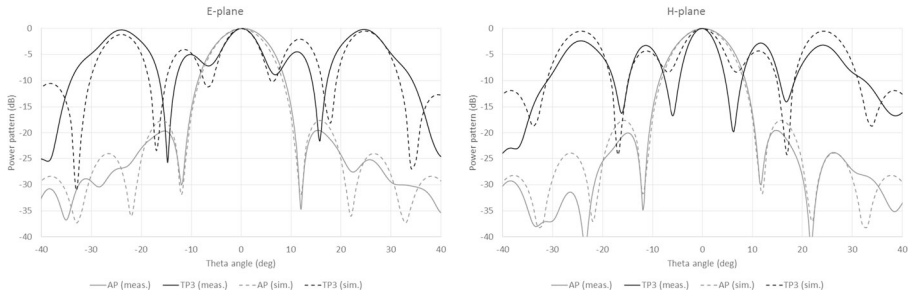


**Fig. 13** Normalized power patterns (from  $-40$  to  $0$  dB) obtained in the case of the three-coronae TP in the  $E$ -plane (left panel) and  $H$ -plane (right panel), for an angular range  $-40^\circ$  to  $40^\circ$  (the angle  $\theta$  refers to the angular separation between the optical axis and the direction of observation). The solid lines represent the measured data (after the NF-FF transformation), while the dashed lines represent the FEKO models. The radiation diagrams of the open pupil (indicated as APerture in the figures) are shown for reference (light-grey curves)

483 the FF along the  $y$ - and  $x$ -axis, respectively (thus corresponding to the vertical and  
 484 horizontal orientations discussed in Appendix A). The radiation diagrams show sev-  
 485 eral interesting features. First of all, the super-resolution effect is clearly visible for  
 486 both TPs, though at different levels, as expected. The FWHM is different along the  
 487 two planes and is a consequence of the slight asymmetry of the radiation diagrams  
 488 in the  $H$ - and  $E$ -planes. Secondly, the number, intensity and position of the side-  
 489 lobes is also different between the two TPs, which is also expected, as discussed in  
 490 Section 2 (see also Ref. [18]). In particular, the four-coronae TP has much lower level  
 491 sidelobes, though the resolution gain,  $G$ , is somewhat lower compared to the three-  
 492 coronae TP. Finally, the normalized power patterns in Figs. 13 and 14 do not show  
 493 that the radiation diagrams of the TPs lie several dBs below the intensity level of the  
 494 open pupil. Therefore, before TPs can be used effectively on a radio telescope their  
 495 overall efficiency must be increased (see also Section 6).

496 When comparing the measured (and NF to FF transformed) FF of the TPs with the  
 497 simulated FF from FEKO, we note from Figs. 13 and 14 that the simulated FF of the  
 498 open pupil closely follows the measured field, particularly in the  $H$ -plane. However,

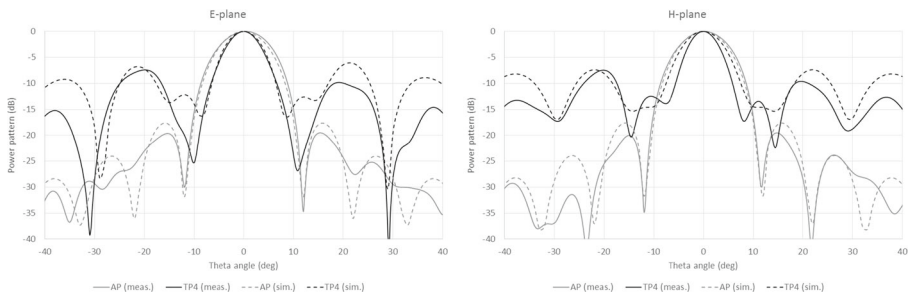


**Fig. 14** Same as Fig. 13 for the four-coronae TP

in the case of the TPs we can note some discrepancies between the measured and simulated fields, which are more evident in the  $H$ -plane. At present, we do not have a convincing explanation of as to why in the  $H$ -plane we simultaneously observe a better agreement between the measured and simulated FF of the open pupil, and a larger discrepancy in the case of the composite pupils. A tentative explanation could be that the dielectric coronae are not modeled with sufficient accuracy by our numerical simulations in FEKO. In all cases we can also note an increasingly larger discrepancy between the measured and modeled sidelobes at larger observing angles. This effect, however, is better known and is associated with the truncation effect discussed in Appendix A.

Given all uncertainties and limitations in both the experimental measurements and numerical simulations, we think that the agreement between the measured and simulated FF is reasonably good, and confirms the ability of a discrete TP to achieve the super-resolution effect even in the absence of the required amplitude apodization, as previously discussed in Section 2. These measurements also show that it is indeed possible to achieve a trade-off between the super-resolution effect and the sidelobes level when a larger number of coronae is used in the design of the TP.

## 6 Conclusions

“Toraldos Pupils”, or variable transmittance filters, introduced by G. Toraldo di Francia in 1952 [23, 24], represent a viable technique to achieve super-resolution, i.e., an angular resolution beyond the classical diffraction limit, in the microwave range. One of the most important characteristic of the TP is its simplicity and ease of fabrication. In order to investigate the possibility to apply these techniques to filled-aperture radio telescopes, we have first performed a series of extensive EM numerical simulations [18] at a frequency of 20 GHz, which represents a trade-off between the computing time required by the EM simulations and the size and separations of the microwave components in units of wavelengths. The simulated FFs confirm that a partial super-resolution effect can be achieved even without the amplitude apodization required by the ideal optical model. We have also used additional EM simulations to more accurately model the launcher (rectangular feedhorn) and the spatial sampling in the NF by the probe.

We have then carried out laboratory measurements of the diffracted NFs by different TPs and compared them with the corresponding diffraction pattern of a circular open pupil. We first performed a series of preliminary tests, mainly devoted to measure various sources of noise and scattering, and then carried out planar scanings of the NF, measuring both the copolar and cross-polar components of the fields. The NF was then transformed into the FF and we detect the super-resolving effect in both ranges. Comparing our results in the FF with the FEKO numerical simulations, we find in general a good agreement. Our sensitivity is good enough to measure the sidelobes, allowing us to compare the level and number of sidelobes for the two TPs under test. Our measurements confirm the results of the first experiments in the microwave range [14, 20] and, in particular, they show that the super-resolution effect is achieved with both three- and four-coronae discrete TPs. The different resolution

542 gain,  $G$ , and sidelobes obtained with the two TPs confirm that the number and geom-  
543 etry of the coroneae can be used to achieve a trade-off between  $G$  and the sidelobes  
544 relative intensity and position. This is important if a specific device including a TP  
545 should be designed to operate on a radio telescope.

546 Overall, our investigation confirms the super-resolving TP proof of concept. How-  
547 ever, before TPs can be used efficiently on a radio telescope several problems must  
548 be addressed and solved. The main problem is that a variable transmittance filter  
549 should ideally be placed at the entrance pupil of a filled-aperture telescope, i.e., the  
550 primary reflector for classical two-mirrors telescopes. As this is clearly impractical  
551 (unless an active primary surface is available), a viable option is to place the TP at  
552 an *image* of the entrance pupil. This image can be generated through the use of a  
553 collimator, which also couples the TP device to, e.g., an existing receiver of a radio  
554 telescope. This and other design issues will be discussed in a forthcoming paper that  
555 will describe the preliminary design of a prototype TP optical system to be mounted  
556 on the 32-m Medicina antenna in Italy<sup>5</sup> [17].

557 Another important problem that needs further analysis is that the gain in angular  
558 resolution, obtained by the reduction in size of the main lobe, may be offset by the  
559 increase in intensity of the sidelobes and the decrease in the aperture efficiency (or  
560 antenna gain [16]) of the radio telescope. By using pupils with an array of concen-  
561 tric annuli, or even a *continuous* TP (Olmli et al., in prep.), the PSF can be tailored  
562 in such a fashion that one can get a narrow central beam surrounded by neighbor-  
563 ing sidelobes of low intensity. The sidelobe level and position with respect to the  
564 optical axis are important especially in mapping applications. However, in this case  
565 an alternative solution can be the application of deconvolution algorithms to remove  
566 the high sidelobes from the final map [21]. We think that the loss in the aperture  
567 efficiency measured in our laboratory experiments can be mitigated by the use of  
568 efficient global optimization algorithms in the design of super-resolving pupil filters,  
569 as well as by the use of metamaterials.

570 **Acknowledgements** We gratefully acknowledge the contribution of the Ente Cassa di Risparmio di  
571 Firenze (Italy) for supporting this research. We also wish to thank G. Cauzzi (INAF-OAA) for providing  
572 us with some of the essential mechanical components used in our laboratory measurements, L. Carbonaro  
573 (INAF-OAA) for helpful suggestions regarding the mechanical setup and A. Ignesti (CNR-IFAC) for  
574 valuable suggestions on how to perform the measurements in the anechoic chamber.

## 575 **Appendix A: Plane-rectangular NF-FF transformation**

576 Among the NF-FF transformation techniques (planar, cylindrical or spherical), the  
577 plane-rectangular scanning is the simplest and most efficient from the analytical  
578 and computational viewpoints. Such a technique is particularly suitable for highly  
579 directive antennas since the pattern can be reconstructed only in a cone with an  
580 apex angle less than  $180^\circ$ . In the plane-rectangular scanning (Fig. 15), the probe is  
581 mounted on a  $x$ - $y$  positioner so that it can measure the NF amplitude and phase

---

<sup>5</sup><http://www.med.ira.inaf.it/>.

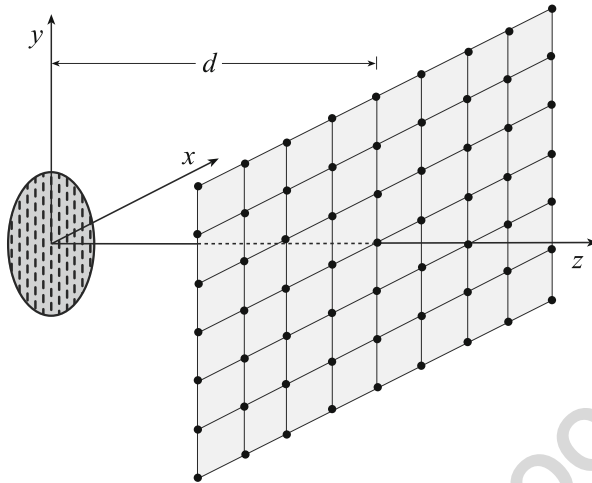


**Fig. 15** Schematics of the plane-rectangular scanning

on a plane-rectangular grid. From these data, measured for two orthogonal orientations (horizontal,  $H$ , and vertical,  $V$ ) of the probe, or equivalently the transmitting feedhorn (by applying a  $90^\circ$  rotation around the longitudinal axis in the second set), and taking into account the probe spatial response, one can compute the antenna FF pattern [7, 19].

It can be easily recognized that the NF tangential components of the field ( $E_x$  and  $E_y$ ) cannot be obtained when performing the measurement by means of a real probe. In fact, the probe sees the center of the diffracting pupil (which constitutes our “antenna under test”, or AUT) from different directions when moving in the scanning plane. Moreover, even at a fixed position the probe sees each point of the AUT from a different angle. As a consequence, the FF of the AUT cannot be accurately recovered from the measured NF data by employing the uncompensated NF-FF transformation. The basic theory of probe compensated NF measurements on a plane as proposed in Refs. [8, 19] is based on the application of the Lorentz reciprocity theorem. The key relations in the reference system used in the present work are:

$$E_\theta(\theta, \phi) = \frac{1}{\Delta} [I_H E_{\phi_V}'(\theta, -\phi) - I_V E_{\phi_H}'(\theta, -\phi)] \tag{2}$$

$$E_\phi(\theta, \phi) = \frac{1}{\Delta} [I_H E_{\theta_V}'(\theta, -\phi) - I_V E_{\theta_H}'(\theta, -\phi)] \tag{3}$$

where:

$$\Delta = E_{\theta_H}'(\theta, -\phi) E_{\phi_V}'(\theta, -\phi) - E_{\theta_V}'(\theta, -\phi) E_{\phi_H}'(\theta, -\phi) \tag{4}$$

and

$$I_{V,H} = A \cos \theta e^{j\beta d \cos \theta} \times \int_{-\infty}^{\infty} \int_{-\infty}^{\infty} V_{V,H}(x, y) e^{j\beta x \sin \theta \cos \phi} e^{j\beta y \sin \theta \sin \phi} dx dy \tag{5}$$

599 where  $A$  is a constant and  $\beta$  is the free-space wavenumber. Namely, the antenna  
 600 FF is related to: (i) the 2D Fourier transforms  $I_V$  and  $I_H$  of the output voltages  $V_V$   
 601 and  $V_H$  of the probe for the two independent sets of measurements; and (ii) the FF  
 602 components  $E_{\theta'_V}$ ,  $E_{\phi'_V}$  and  $E_{\theta'_H}$ ,  $E_{\phi'_H}$  radiated by the probe and the rotated probe,  
 603 respectively, when used as transmitting antennas. According to Ref. [25], the FF  
 604 components of the electric field,  $E_{\theta'_V}$ ,  $E_{\phi'_V}$ , radiated by an open-ended rectangular  
 605 waveguide (of sizes  $a'$  and  $b'$  along the  $x$  and  $y$  axis, respectively) excited by a TE<sub>10</sub>  
 606 mode are:

$$E_{\theta'_V} = f_{\theta}(\theta; a', b') \sin \phi \frac{e^{-j\beta r}}{r} \tag{6}$$

607

$$E_{\phi'_V} = f_{\phi}(\theta; a', b') \cos \phi \frac{e^{-j\beta r}}{r} \tag{7}$$

608 where the function  $f_{\phi}(\theta; a', b')$  is discussed in Ref. [25]. Similar equations can be  
 609 found for the  $E_{\theta'_H}$ ,  $E_{\phi'_H}$  field components.

610 According to (5), in order to obtain the FF pattern all over the hemisphere in  
 611 front of the AUT, the measurement plane should be infinite but, of course, this is  
 612 not possible in a practical setup. The dimension of the plane should be such that the  
 613 field becomes negligible at its edges, thus, minimizing the error associated with this  
 614 truncation. Due to this so-called truncation error, the calculated FF using the planar  
 615 NF data is valid only up to a critical angle  $\theta_c \simeq 16.7^\circ$  outward from the aperture of  
 616 the AUT (see Fig. 16):

$$\theta_c = \arctan \left( \frac{L - D}{2d} \right). \tag{8}$$

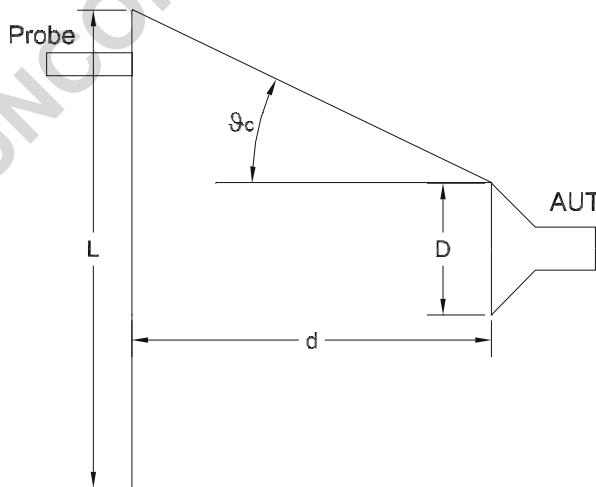


**Fig. 16** Definition of the critical angle,  $\theta_c$ , and its relation to the geometry of the measurement setup. From Fig. 9,  $D = 9$  cm and  $d = 10$  cm

## References

617

1. Born, M., Wolf, E.: Principles of Optics, 7th edn. (1999) 618
2. Cagigal, M.P., Canales, V.F., Oti, J.E.: Design of Continuous Superresolving Masks for Ground-based Telescopes. *Publ. Astron. Soc. Pac.* **116**, 965–970 (2004). doi:[10.1086/425592](https://doi.org/10.1086/425592) 619
3. Canales, V.F., de Juana, D.M., Cagigal, M.P.: Superresolution in compensated telescopes. *Opt. Lett.* **29**, 935–937 (2004). doi:[10.1364/OL.29.000935](https://doi.org/10.1364/OL.29.000935) 620
4. Cox, I.J., Sheppard, C.J.R., Wilson, T.: Reappraisal of arrays of concentric annuli as superresolving filters. *J. Opt. Soc. Am.* **72**, 1917–1983 (1982) 621
5. de Juana, D.M., Oti, J.E., Canales, V.F., Cagigal, M.P.: Design of superresolving continuous phase filters. *Opt. Lett.* **28**, 607–609 (2003). doi:[10.1364/OL.28.000607](https://doi.org/10.1364/OL.28.000607) 622
6. Goldsmith, P.F.: Quasioptical Systems (1998) 623
7. Joy, E., Paris, D.: Spatial sampling and filtering in near-field measurements. *IEEE Trans. Antennas Propag.* **20**, 253–261 (1972). doi:[10.1109/TAP.1972.1140193](https://doi.org/10.1109/TAP.1972.1140193) 624
8. Joy, E.B., Leach, Jr., W.M., Rodrigue, G.P., Paris, D.T.: Applications of probe-compensated near-field measurements. *IEEE Trans. Antennas Propag.* **26**, 379–389 (1978). doi:[10.1109/TAP.1978.1141856](https://doi.org/10.1109/TAP.1978.1141856) 625
9. Kellerer, A.: Beating the diffraction limit in astronomy via quantum cloning. *Astron. Astrophys.* **561**, A118 (2014). doi:[10.1051/0004-6361/201322665](https://doi.org/10.1051/0004-6361/201322665) 626
10. Kim, H., Bryant, G.W., Stranick, S.J.: Superresolution four-wave mixing microscopy. *Opt. Express* **20**, 6042 (2012). doi:[10.1364/OE.20.006042](https://doi.org/10.1364/OE.20.006042) 627
11. Liu, L., Wang, G.: Designing superresolution optical pupil filter with constrained global optimization algorithm. *Optik* **119**, 481–484 (2008) 628
12. Martinez-Corral, M., Caballero, M.T., Stelzer, E.H.K., Swoger, J.: Tailoring the axial shape of the point spread function using the Toraldo concept. *Opt. Express* **10**, 98 (2002) 629
13. May, J., Jennetti, T.: Telescope Resolution Using Negative Refractive Index Materials. In: *UV/Optical/IR Space Telescopes: Innovative Technologies and Concepts, Proceedings of the SPIE*, vol. 5166, p. 220 (2004) 630
14. Mugnai, D., Ranfagni, A., Ruggeri, R.: Pupils with super-resolution. *Phys. Lett. A* **311**, 77–81 (2003). doi:[10.1016/S0375-9601\(03\)00445-6](https://doi.org/10.1016/S0375-9601(03)00445-6) 631
15. Neil, M.A.A., Wilson, T., Juskaitis, R.: A wavefront generator for complex pupil function synthesis and point spread function engineering. *J. Microsc.* **197**, 219 (2000) 632
16. Olmi, L., Bolli, P.: Ray-tracing and physical-optics analysis of the aperture efficiency in a radio telescope. *Appl. Opt.*, 46 (2007) 633
17. Olmi, L., Bolli, P., Carbonaro, L., Cresci, L., Mugnai, D., Natale, E., Nesti, R., Panella, D., Roda, J., Zacchioli, G.: Design of Super-Resolving Toraldo Pupils for Radio Astronomical Applications. In: *Proceedings of the XXXII URSI General Assembly and Scientific Symposium (2017)*. submitted 634
18. Olmi, L., Bolli, P., Cresci, L., Mugnai, D., Natale, E., Nesti, R., Panella, D., Stefani, L.: Super-resolution with Toraldo Pupils: Analysis with Electromagnetic Numerical Simulations. In: *Ground-Based and Airborne Telescopes VI, Proceedings of the SPIE*, vol. 9906 (2016) 635
19. Paris, D.T., Leach Jr., W.M., Joy, E.B.: Basic theory of probe-compensated near-field measurements. *IEEE Trans. Antennas Propag.* **26**, 373–379 (1978). doi:[10.1109/TAP.1978.1141855](https://doi.org/10.1109/TAP.1978.1141855) 636
20. Ranfagni, A., Mugnai, D., Ruggeri, R.: Beyond the diffraction limit: Super-resolving pupils. *J. Appl. Phys.* **95**, 2217–2222 (2004). doi:[10.1063/1.1644026](https://doi.org/10.1063/1.1644026) 637
21. Roy, A., Ade, P.A.R., Bock, J.J., Brunt, C.M., Chapin, E.L., Devlin, M.J., Dicker, S.R., France, K., Gibb, A.G., Griffin, M., Gundersen, J.O., Halpern, M., Hargrave, P.C., Hughes, D.H., Klein, J., Marsden, G., Martin, P.G., Maukopf, P., Netterfield, C.B., Olmi, L., Patanchon, G., Rex, M., Scott, D., Semisch, C., Truch, M.D.P., Tucker, C., Tucker, G.S., Viero, M.P., Wiebe, D.V.: Deconvolution of Images from BLAST 2005: Insight into the K3-50 and IC 5146 Star-forming Regions. *Astrophys. J.* **730**, 142 (2011). doi:[10.1088/0004-637X/730/2/142](https://doi.org/10.1088/0004-637X/730/2/142) 638
22. Silver, S.: *Microwave Antenna theory and Design*. McGraw-Hill Company (1949) 639
23. Toraldo di Francia, G.: vol. 9 (1952) 640
24. Toraldo di Francia, G.: *Atti Fond. Giorgio Ronchi* **7**, 366 (1952) 641
25. Yaghjian, A.D.: Approximate formulas for the far field and gain of open-ended rectangular waveguide. *IEEE Trans. Antennas Propag.* **32**, 378–384 (1984). doi:[10.1109/TAP.1984.1143332](https://doi.org/10.1109/TAP.1984.1143332) 642
26. Zhang, X., Liu, Z.: Superlenses to overcome the diffraction limit. *Nat. Mater.* **7**, 435–441 (2008). doi:[10.1038/nmat2141](https://doi.org/10.1038/nmat2141) 643

618  
619  
620  
621  
622  
623  
624  
625  
626  
627  
628  
629  
630  
631  
632  
633  
634  
635  
636  
637  
638  
639  
640  
641  
642  
643  
644  
645  
646  
647  
648  
649  
650  
651  
652  
653  
654  
655  
656  
657  
658  
659  
660  
661  
662  
663  
664  
665  
666  
667  
668  
669  
670  
671  
672

## AUTHOR QUERIES

### **AUTHOR PLEASE ANSWER ALL QUERIES:**

- Q1. Please check presentation of reference citation in abstract if correct.
- Q2. Please check captured affiliations if presented correctly.
- Q3. Please check captured figure 2 if presented correctly.
- Q4. Please check Ref. 4 if captured and presented correctly.
- Q5. Please provide article title for References 23 and 24.